

Hubble Space Telescope prescription retrieval

David Redding, Phil Dumont, and Jeff Yu

Prescription retrieval is a technique for directly estimating optical prescription parameters from images. We apply it to estimate the value of the Hubble Space Telescope primary mirror conic constant. Our results agree with other studies that examined primary-mirror test fixtures and results. In addition they show that small aberrations exist on the planetary-camera repeater optics.

Introduction

Initial images from the wide field planetary camera (WFPC) and the faint-object camera indicated that the primary mirror of the Hubble Space Telescope (HST) was figured incorrectly. Two sets of studies involving numerous investigators were performed to determine the primary-mirror conic-constant value. They derived apparently inconsistent results. The archival data studies examined the test hardware and results to determine problems caused by fabrication errors, deriving values for a primary-mirror conic constant of -1.01378 ± 0.0003^1 . The phase-retrieval studies^{2,3} processed images to determine exit-pupil phases by using a variety of techniques. We analyzed the converged phase solution to determine the degree of spherical aberration. The conic constant is then estimated on the critical assumption that the spherical aberration is due to only the primary mirror. The resulting estimate of the conic constant (averaged among seven different study results) is -1.0148 ± 0.00038 .

We employed a third approach, which Si Brewer (PAGOS Corporation, San Simeon, Calif.) called prescription retrieval. Like phase retrieval, prescription retrieval is an image-inversion technique, where parameters are varied in a mathematical model of the optical system until that model produces images that match the actual images. It differs from phase retrieval in the nature of the model: prescription retrieval uses a full ray trace and diffraction model rather than a single-plane exit-pupil phase model. The model is parameterized with prescription vari-

ables such as the conic constants and alignments of the 13 optical elements, which enable the direct estimation of these parameters from the images.

We estimate the primary mirror conic constant to be -1.01386 ± 0.0002 based on a limited set of images taken with planetary camera 6 (PC6). This result is in agreement with the archival-data studies but not with the phase-retrieval studies. Our results also show that significant aberrations exist in the relay-camera primary and secondary mirrors. These changes impact the pupil phase map. Estimates of other key design parameters are listed below.

To compare our results with the phase-retrieval studies, we computed the total spherical aberration z_{11} in the exit pupil based on the converged prescription results for a particular image set. The resulting z_{11} is $-0.2943 \mu\text{m}$ rms. This agrees with an average value of spherical aberration of -0.2906 ± 0.0061 computed by the Shao group.³ The phase derived from our converged prescription agrees with the phase-retrieval code to within a 0.0002 level of the equivalent primary-mirror conic constant.

Our conclusion is that the archival data studies derived the correct conic constant. We believe that the phase-retrieval studies correctly determined the exit-pupil phase map but that the key assumption that the spherical aberration component was due to only the primary mirror is in error. Estimates of the conic constant derived on that basis are in error. Our study was not completed. Further work would improve the estimates of the primary-mirror conic constant and other parameters.

Prescription Retrieval

Problem Statement

Given a set of images and a good initial estimate of the optical prescription of the HST/WFPC system, one can determine the HST primary-mirror conic con-

All authors are with the Jet Propulsion Laboratory, California Institute of Technology, Pasadena, California 91109. D. Redding is with the Charles Stark Draper Laboratory.

Received 16 December 1991.

0003-6935/93/101728-09\$05.00/0.

© 1993 Optical Society of America.

stant to an accuracy of ± 0.0005 . This level of accuracy is required for the design of the replacement WFPC2, which is to be flown in 1993.

Solution Approach

Our prescription-retrieval approach is a model-matching technique based on a highly detailed computer model of the HST/WFPC system. This model generates images based directly on the optical design variables of the HST/WFPC6 system. The solution code iterates these parameters, i.e., the optical prescription, until the model accurately predicts the observed images (Fig. 1). The computer model uses a hybrid ray trace and diffraction approach. The ray trace is the only way to determine accurately the systematic aberrations induced by field position or element misalignments. The diffraction produces the actual images. The model includes the effects of detector sampling, detector noise, and spacecraft jitter.

Perturbations of the elements that induce aberrations (e.g., secondary-mirror misalignment producing coma and astigmatism) are determined explicitly so as to separate them from the effects of the primary-mirror figure error. The starting point for our solutions was provided by the Code V as-built prescription determined for the on-orbit system by the Hubble Aberration Recovery Program (HARP). This prescription uses element parameters taken from piece-part drawings. We derived element positions from an alignment procedure, as simulated using Code V. The primary conic was set by early results of the archival and phase-retrieval studies.

We coded the model by using the Subroutine Controlled Optics Modeling Package (SCOMP) described below. A total of 65,000 rays are traced through the HST/PC6 system for each 512×512 image. The diffracted point-source images are computed by SCOMP based on phase and obscuration information derived from the ray trace.

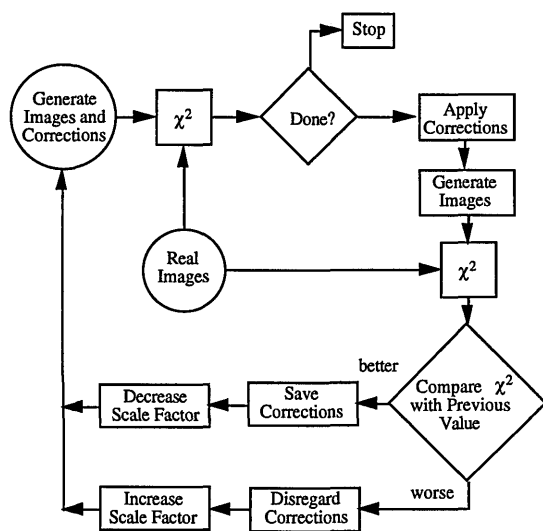


Fig. 1. Prescription-retrieval solution algorithm.

The solution code that manipulates the model to match the images is based on the Levenberg-Marquardt implementation of a nonlinear least-squares (NLLS) algorithm. NLLS finds the best fit between simulated images produced by a parameterized model of the optical system and on-orbit images. The best fit is defined in the least-squares sense by minimizing the sum of the square of pixel differences between simulated and on-orbit images.

Optical Model of the HST/WFPC

HST/WFPC6 Optical System

The images that we used were taken specifically for diagnostic purposes as part of HARP. They were taken on both sides of focus (the focus setting is altered by the piston motion of the secondary mirror) and in several different field positions to expose image features such as the secondary-mirror spiders, the primary-mirror pads, the repeater-camera spiders, and the spherical aberration rings. Images were taken in several of the WFPC's, but those taken with PC6 were the clearest. We used several PC6 images.

The basic optical prescription we used as a starting point for our solutions was derived from the as-flown prescription developed for the HARP.⁴ The HST/WFPC6 beam train is sketched in Fig. 2. It consists of 13 optical elements modeled by using 16 surfaces as listed in Table 1.

The main system stop is at the primary mirror. The light beams from objects at different field points are represented as collimated bundles of rays (planar wave fronts) centered on the primary mirror. The beam is obscured at the secondary-mirror spiders, the primary-mirror pads, and at the relay secondary-mirror spiders, which are three-sided. These obscurations are illustrated in the pupil intensity maps given below (Figs. 3–6). The aberrated HST/WFPC6 system exit pupil is located ~ 66 mm in front of the CCD detector.

The HARP images that we used for our solutions were taken at three wavelengths: 487, 631, and 889 nm. The images were provided as cropped 256×256 sections of the full 800×800 CCD field.

The size of the image pixels ($15 \mu\text{m}$) plus the need to sample the aberrated wave front adequately at the exit pupil set the optical model code size parameters. The final far-field diffraction propagation is required to scale to a wave-front grid size that is smaller than

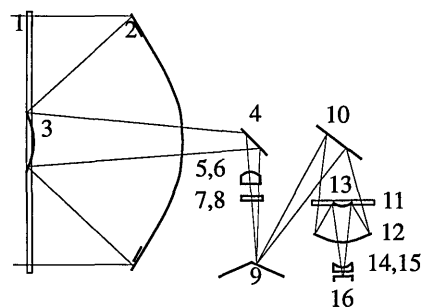


Fig. 2. HST/WFPC beam train.

Table 1. HST/WFPC6 Optical Elements

Element	Description
1	HST secondary spiders
2	HST primary mirror
3	HST secondary mirror
4	WFPC pickoff mirror
5,6	WFPC cork lens
7,8	WFPC filter
9	WFPC pyramid mirror
10	PC6 fold mirror
11	PC6 secondary spiders
12	PC6 primary mirror
13	PC6 secondary mirror
14,15	PC6 field flattener lens
16	PC6 CCD detector

the actual pixel size. This plus the need to fill the 256×256 pixel array led to a requirement that the optical model use a 512×512 diffraction grid. Experiments with the guard bands used to avoid aliasing in the diffraction calculations showed that the best compromise between aliasing and sampling requirements left a central 283×283 for the beam. The optical modeling code was therefore set up to trace 66,000 rays to determine beam phases for the 512×512 diffraction calculations.

Controlled Optics Modeling Package

For prescription retrieval the optical modeling code is called many times to generate images and pixel-by-pixel numerical derivatives of images. This, plus our desire that the code run on desktop work stations, imposes a requirement that the modeling code be as computationally efficient as possible.

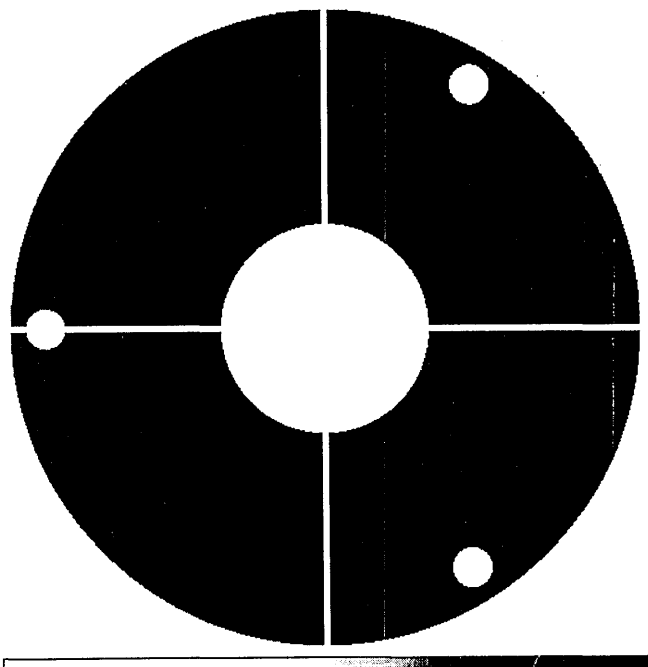


Fig. 3. Intensity at the HST secondary mirror.

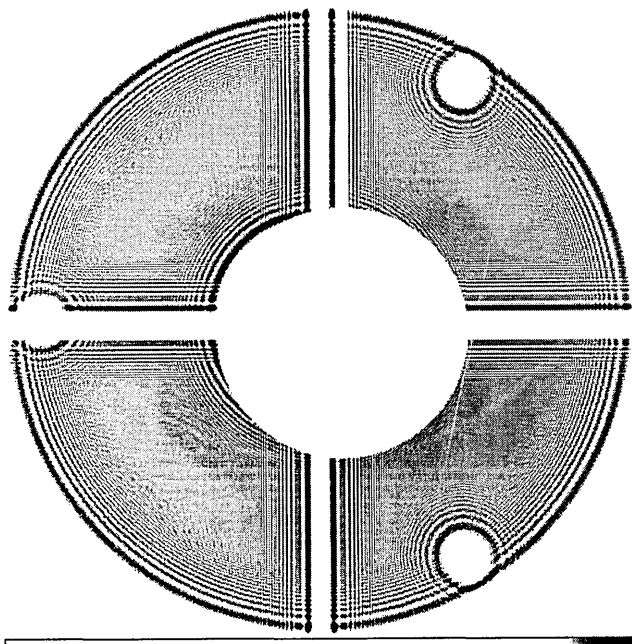


Fig. 4. Intensity at PC6 repeater spiders.

We used the controlled optics modeling package (COMP)^{5,6} to provide the optical model. COMP is a stand-alone optical modeling computer code whose capabilities include geometric optics, physical optics including multiplane diffraction, image simulation, differential ray tracing, sensitivity analysis, and linear optical model building. We used an in-line subroutine version (SCOMP) to generate images for our parameter solver program.

COMP provides a computationally efficient general ray-trace capability through the use of a set of coordinate-free ray-trace equations.⁷ The computa-

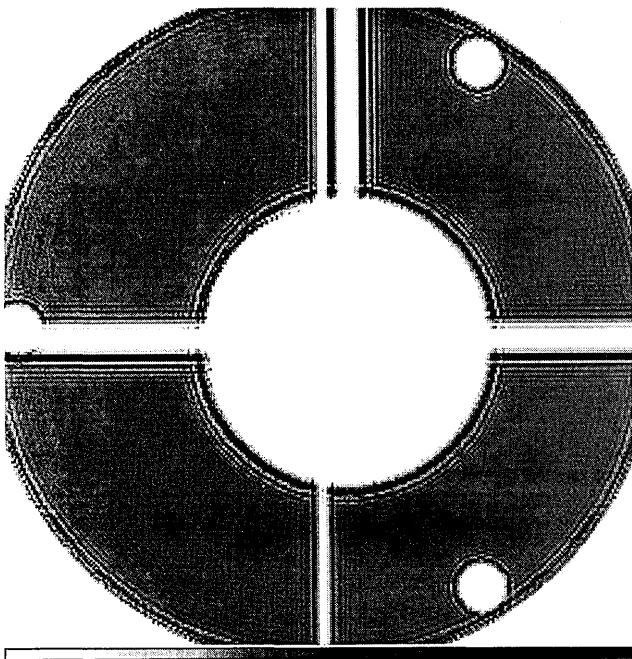


Fig. 5. Intensity at the PC6 exit pupil.

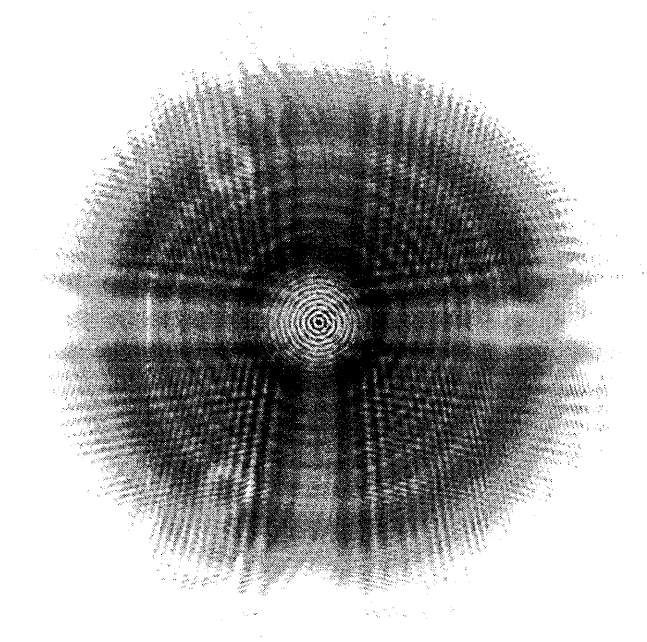


Fig. 6. Image intensity at the PC6 detector (five-plane model, no noise).

tional efficiency results from working in a single coordinate system, elimination of transcendental functions, elimination of extraneous surfaces, and an optimized code.

To generate images COMP defines a mapping from a bundle of rays to pixels in a complex amplitude matrix that represents the light beam. The propagation of the complex amplitude is driven by the exact phases determined from the ray trace. This approach correctly computes induced aberrations and pupil obscurations. COMP allows the user to specify the type of diffraction propagation that is to be used at each point in the beam train. It provides Fresnel near-field and far-field propagators as well as a geometric propagator, which updates phase only based on the optical path length and is used in areas where the Fresnel assumptions are violated. The user sets up reference surfaces to define different propagation regions. The user can define a full surface-to-surface multiplane diffraction model or a single-plane exit-pupil diffraction model to generate images.

Comparison of Single- and Multiple-Plane Models

We computed most of the results presented here by using a single-plane model. The single-plane models were used mainly because we ran out of time before completely implementing the multiplane version of SCOMP. In this section we compare an image generated by the single-plane model with one generated by a more rigorous multiplane model. The two images match quite closely. Nonetheless, as Fienup² showed, small differences resulting from diffraction effects can have an appreciable effect on estimates of the conic constant.

The single-plane model uses a single far-field diffraction calculation from the exit pupil to the detector. The multiple-plane model uses five planes of diffraction: four near-field propagations in the beam train and a final far-field propagation. The SCOMP computation sequence for each model is as follows (this process corresponds to the Generate Images function of Fig. 1):

- (1) Apply element perturbations to the base prescription. Exact kinematical relations are used to rotate and translate the optical elements and input beam, and deformations and other effects are applied in response to prescription parameter changes determined by the prescription-retrieval code.
- (2) Compute a new exit pupil location.
- (3) (Multiplane model) compute new diffraction reference surfaces.
- (4) Trace rays and propagate the complex amplitude matrix.
- (5) Resample the image to the detector pixels and add jitter. Noise is added for display purposes only. For images generated during the solution process, the noise is used only in the calculation of the χ^2 fitting error metric.

Figures 3–6 illustrate the result of this process for a particular image. They show the light intensities at three locations in the multiplane model, after each obscuring surface and the image at the detector. The multiplane image is to be compared with the single-plane image of Fig. 7. These images were created by using a 1024×1024 version of COMP. (Only the central 512×512 is displayed.) No noise or jitter is added.

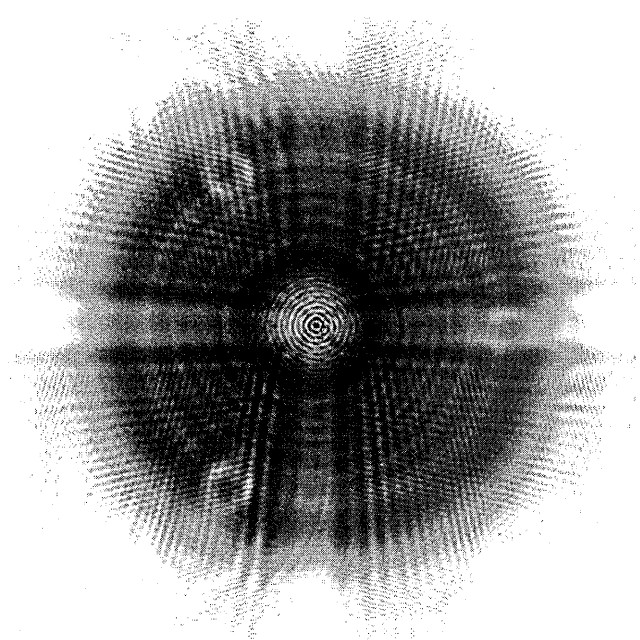


Fig. 7. Image intensity at the PC6 detector (one-plane model, no noise).

Noise Models

The HARP images are corrupted by noise and jitter. We explicitly account for these effects so as to minimize the distortion of image features. The three phenomena included in our noise model are the detector sampling, telescope pointing jitter, and background noise.

The on-orbit images are recorded with a CCD detector. The actual CCD detectors have a fixed pixel size (15.24 mm and square), which in general is not equal to the SCOMP complex amplitude mesh size. There is also an offset between the centers of the wave-front grid and the detector pixel grid. These effects are accounted for by resampling the computed intensity pattern onto a physically correct pixel grid. The centroid of the image relative to the pixel grid is optimized by the parameter solver.

Jitter, or the random or quasirandom vibration of the Hubble telescope during an exposure, results in smearing the detected image with a consequent loss of high-spatial-frequency information. If the temporal frequency of the jitter is high compared with the image sampling/integration rate, we can simulate the smearing using convolution methods. This approach assumes that the jitter pointing error is a zero-mean Gaussian random process.

We used this approach by computing the standard deviation for the probability density function (PDF) of the jitter distribution from fine guidance sensor data. The two-dimensional function used to represent the jitter PDF is

$$P(x, y) = \exp \left[-\frac{1}{2} \left(\frac{x^2}{\sigma_x^2} + \frac{y^2}{\sigma_y^2} + \frac{xy}{\sigma_{xy}} \right) \right]. \quad (1)$$

The jittered image is the convolution of the jitter PDF with the instantaneous point spread function produced by the optical system.

The background noise includes effects associated with image preprocessing (variances in the flat-field correction and the UV flood illumination of the CCD), the CCD read noise, and the Poisson noise of the detected signal in each pixel from the star. The noise in each pixel is estimated from

$$s(DN) = [(DN + 2P + 2R) + \text{var}(F)(DN + 2P + 2R)]^{0.5}, \quad (2)$$

where DN is the signal count in each CCD pixel, P is the flood illumination value, R is the CCD read noise value, and F is the flat-field factor. This noise term is not added directly to the images. Rather it is used to set the uncertainty values used to compute the χ^2 fitting error metric.

Nonlinear Least-Squares Parameter Solver

Algorithm

Images are nonlinear functions of perturbations to the optical prescription, even though the complex amplitudes from which the images are computed are

nearly linear functions of those perturbations. This is because the intensity is the modulus squared of the amplitude, and all phase information is lost in the squaring. As a result an iterative algorithm is required to determine prescription parameters from intensity data.

For prescription retrieval we use a NLLS approach based on the Levenberg-Marquardt algorithm.^{3,8} NLLS, like linear least squares, is based on the maximum-likelihood hypothesis, which states that the most likely values of a set of parameters describing a system (in our case the HST/WFPC optical system) are those that minimize the weighted squared differences in the computed and actual images. The weighting is supplied by the variance of the signal in each datum. The metric to be minimized is the χ^2 :

$$\chi^2 = \sum_{i=1}^N \left[\frac{y_i - y \text{ mod}_i(\vec{a})}{\sigma_i} \right]^2. \quad (3)$$

Here y_i is the intensity value of the i th real image pixel; $y \text{ mod}_i$ is the intensity value of the i th simulated image pixel (computed by SCOMP), a function of the current parameter vector \vec{a} ; σ_i is the estimate of the variance in the i th image pixel based on the noise calculations described above; and N is the total number of image pixels ($N = \text{number of images} \times \text{number of pixels/image}$).

The NLLS algorithm assumes that the problem in the neighborhood of the current parameter values takes a quadratic form.⁸ The partials of χ^2 are taken with respect to each parameter to set up a system of linear equations, which is solved for corrections to the current parameter vector estimate. In practice this works well if one is near the correct solution or if the problem is fairly quadratic. The computation of the partials of the χ^2 is extremely computationally intensive; it requires the regeneration of each image in the solution set for each parameter being solved for. This occurs during the Generate Images and Corrections block of Fig. 2.

The Levenberg-Marquardt implementation of NLLS introduces a scaling factor that changes the behavior of the algorithm according to the local behavior of the problem. If the quadratic solution fails to improve the χ^2 , the scaling factor is increased, which emphasizes the linear term in the estimation step. The algorithm then behaves more as a steepest descent algorithm does, which is a slower but more robust approach. As the solution nears the correct answer, as indicated by decreasing χ^2 , this scaling term is decreased, so that the algebra yields quadratic minimum-seeking steps for the parameter correction set. This process is sketched in Fig. 2 and reviewed in detail in Ref. 8.

Potential Problems

Several potential pitfalls must be avoided when a NLLS algorithm is used:

(1) Local minima. The NLLS algorithm cannot escape from a local minimum. The likelihood of

being trapped in a local minimum is reduced with a sufficiently diverse data set and a good initial guess.

(2) Inseparable parameters. If two parameters have an identical (or proportionally similar) effect on the images, the contribution of one cannot be distinguished from that of the other. These effects are reduced when we look at different field angles and focus positions.

(3) Inadequate model. Our problem is that not all prescription parameters can be varied at once because of computer-size limits. Such variables as the widths of obscurations were not solved for but can have a significant effect on the image and especially on the value of the χ^2 metric. Similarly, unmodeled changes in the actual HST/WFPC system that are not common to all images in a set add confusion and reduce the quality of the solutions. This type of problem can occur if images are taken at different times, during which the structure of the telescope has changed because of thermal or other effects.

(4) Meaningless parameters. Care must be taken not to confuse important image structure with noise or jitter effects. Solving for these parameters can produce good χ^2 values, but since they carry no information about the optical system, they do not improve the estimates of the prescription parameters.

Results

We obtained results for three sets of images. The first set consists of two 487-nm wavelength HARP images with serial numbers PC6f487n.o1 and PC6f487n.s1. These images are compared with the computer-generated images in Fig. 8–11. The estimated parameter values are given in Table 2. The estimate of the primary-mirror conic K is -1.0139888 ; the χ^2 associated with it is 876,534.

The second set consists of two 889-nm wavelength HARP images, PC6f889n.o1 and PC6f889n.q1.

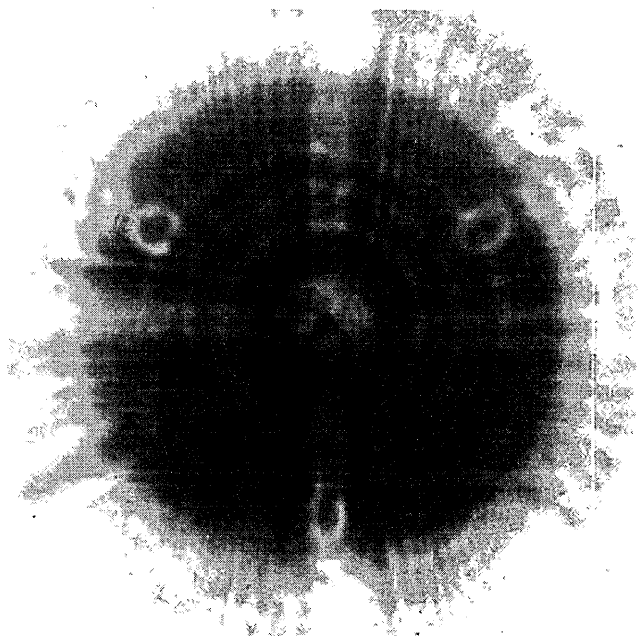


Fig. 9. Actual image: PC6f487.o1.

These images and the computer-generated images are compared in Figs. 12–15. The estimated parameter values are given in Table 3. The estimate of K_c is -1.0137195 ; the χ^2 associated with it is 1,316,730.

The third set consists of one 487-nm wavelength image (PC6f487n.o1) and one 889-nm image from the HARP set, w66407. The estimated parameter values are given in Table 4. The estimate of K_c is -1.0137803 ; the χ^2 associated with it is 2,079,117. To produce a single number estimate of the primary conic constant, we use an average weighted by the χ^2

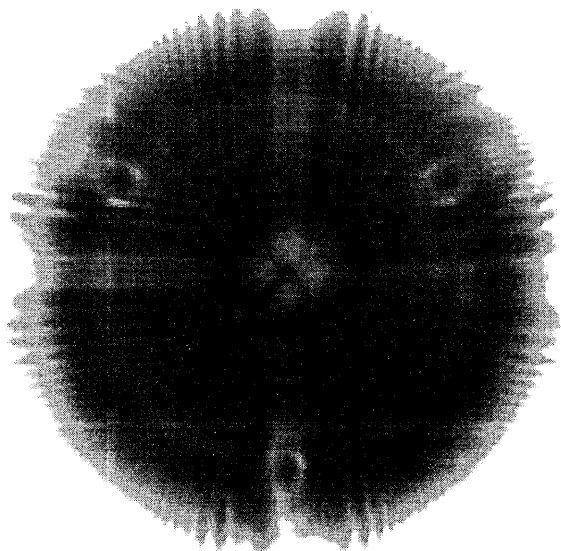


Fig. 8. Simulated image: PC6f487.o1.

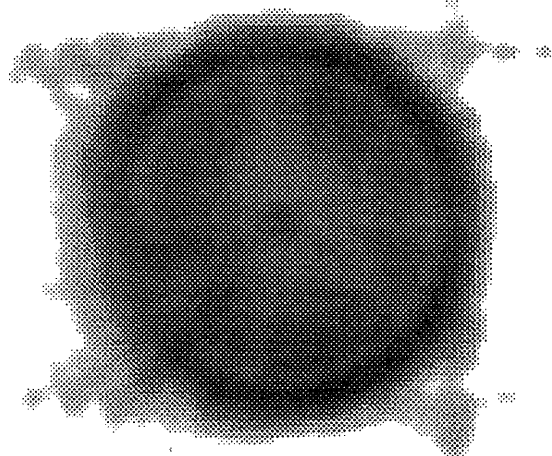


Fig. 10. Simulated image: PC6f487.s1.

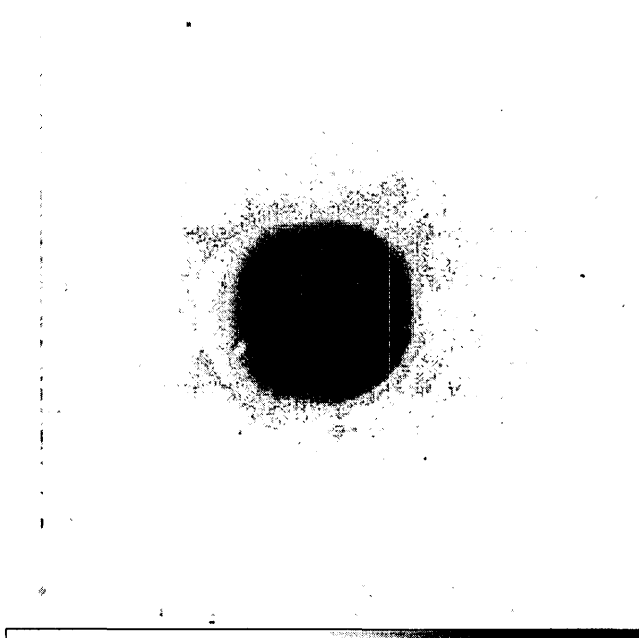


Fig. 11. Actual image: PC6f487.s1.

values:

$$K = \frac{(K_1/\chi_1^2) + (K_2/\chi_2^2) + (K_3/\chi_3^2)}{1/\chi_1^2 + 1/\chi_2^2 + 1/\chi_3^2}. \quad (4)$$

The resulting estimate of K is -1.0138608 .

Discussion

How Good are These Results?

The values of χ^2 for these images are high compared with their ideal values. This indicates that the solutions have not fully converged. A detailed exam-

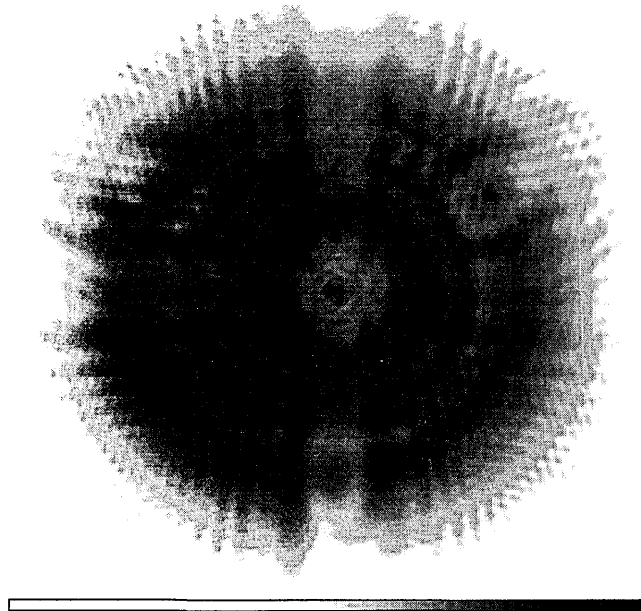


Fig. 12. Simulated image: PC6f889.o1.

ination of the images shows good overall agreement with the actual images, but some details are not perfectly matched. The formal errors for primary mirror conic constant K are quite low ($<10^{-5}$ in each case). This is much smaller than the differences seen when we compare the values of parameters from one image set with those derived from another image set. This also indicates incomplete convergence.

The low formal error is an indication that K can be meaningfully separated from the other parameters by the solution code. This might seem unexpected, since the conic constants of all the mirrors HST/

Table 2. Images Set 1 Estimated Parameters

Parameter	Estimated Change	Nominal Value	Estimated Value
OTA primary-mirror conic	-0.4888453858^{-03}	-1.0135	-1.0139888
Pyramid mirror θz (rad)	0.1365577045^{-02}	0	
Pyramid mirror δx (mm)	0.4047224612^{-01}	0	
Pyramid mirror δy (mm)	-0.206760512	0	
OTA secondary mirror θx (rad)	-0.8518053^{-05}	0	
OTA secondary mirror θy (rad)	-0.45165920^{-04}	0	
OTA secondary mirror δx (mm)	-0.98496539^{-01}	0	
OTA secondary mirror δy (mm)	0.776947890^{-02}	0	
Repeater primary-mirror conic	-0.9242991165^{-02}	-0.305991	-0.315234
Repeater secondary-mirror conic	0.2254954847	-2.49039	-2.2648945

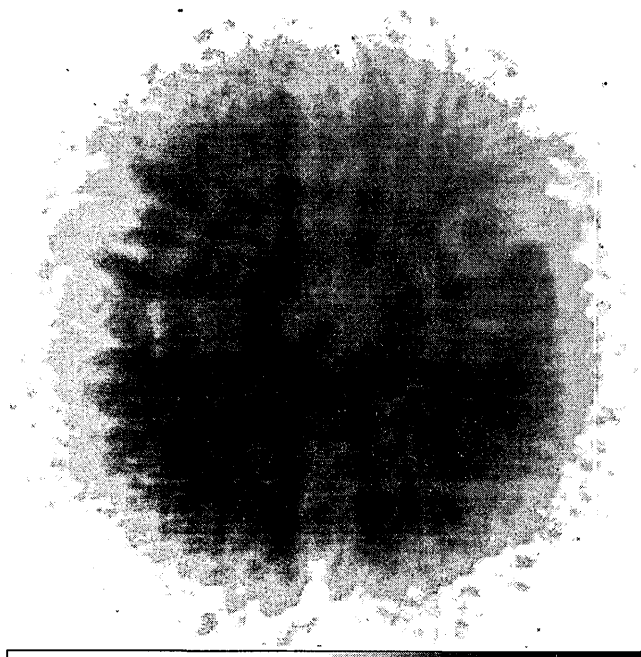


Fig. 13. Actual image: PC6f889.o1.

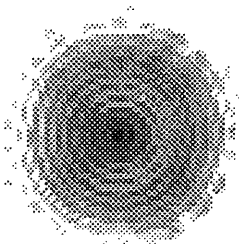


Fig. 14. Simulated image: PC6f889.q1.

WFPC should affect the images in comparable ways in an aligned, on-axis system. We used images that were not taken at the same field point, and the primary mirror aberrations indicate that the optics do not reimagine each other. As a result conic changes on other optics do not have a symmetric effect and can be distinguished from primary-mirror conic K .

How good our estimate is cannot be determined from the formal error calculation until all parameters and images can be included in the same solution run. An approximate bound can be guessed based on the standard deviation of the differences in estimates between runs. This value is 0.0002.

Convergence can be improved in a number of ways:

- (1) More of the prescription parameters can be added to the solution list, which enables a better fit when the existing model is used.
- (2) More images can be processed at the same time.
- (3) We can improve the model by incorporating more details, such as primary-mirror zonal aberrations that have been determined from interferometric test data. Inclusion of the zones was found to reduce χ^2 by one-third in some of the phase-retrieval cases.³
- (4) The multiplane diffraction model could be used.
- (5) Improved initial guesses could be derived from more recent archival data analyses.
- (6) To avoid local minima, one can employ another solution algorithm such as simulated annealing.

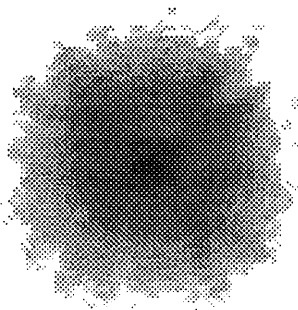


Fig. 15. Actual image: PC6f889.q1.

Table 3. Image Set 2 Estimated Parameters

Parameter	Estimated Change	Nominal Value	Estimated Value
OTA primary-mirror conic	-0.166089^{-03}	-1.0135	-1.013666089
Repeater primary-mirror conic	-0.2166023^{-02}	-0.305991	-0.3062076
Repeater secondary-mirror conic	0.4129071	-2.49039	-2.0774829

Comparison with the Archival Data Studies

Our estimate of the HST primary-mirror conic constant is -1.01386 ± 0.0002 , which agrees with the value determined by the archival data studies. Each of the solved values for K falls within one standard deviation of the archival estimates.

Comparison with the Phase-Retrieval Studies

Our estimate of the conic constant does not agree with estimates derived from the results of the phase-retrieval studies, even though the images we generate compare well (qualitatively) with images generated by the phase-retrieval studies. To investigate this further we picked as a sample case the first 487-nm image set as described above (Figs. 8 and 9). We solved for the spherical aberration component of the pupil phase by using the converged prescription. That value was $-0.2943 \mu\text{m rms}$. This result agrees with the value for spherical aberration of -0.2906 ± 0.0061 that we derived using the Shao group's phase-retrieval code.³

If we compute the conic constant by using the assumption that the spherical aberration is due solely to the primary-mirror conic-constant error, we obtain an estimate for K of -1.01520 . Again this agrees with the estimate for K of -1.01504 ± 0.00027 that we derived from the phase-retrieval results using the same assumption. It disagrees with the value of -1.0139888 estimated directly (Table 2).

The difference lies in the other elements of the beam train. The prescription retrieval results indicate that aberrations that contribute to the total exit-pupil spherical aberration exist not only on the primary mirror but on the relay-camera primary and secondary mirrors as well. This contradicts the assumption that we used in converting the phase to the estimated conic constant.

To sum up, the phase-retrieval studies seem to have correctly determined the exit pupil phase. The

Table 4. Image Set 3 Estimated Parameters

Parameter	Estimated Change	Nominal Value	Estimated Value
OTA primary-mirror conic	-0.280298^{-03}	-1.0135	-1.0137803
Repeater primary-mirror conic	-0.1103011^{-03}	-0.305991	-0.3061013
Repeater secondary-mirror conic	0.3020324	-2.49039	-2.188358

formula used to convert the phase to the primary-mirror conic constant is in error, however, causing the phase-retrieval-based estimates of the conic constant to be in error.

Using Prescription Retrieval for Optical System Alignment

We have investigated prescription retrieval for use in aligning general optical systems. We ran a series of simulated tests on a sample system that consisted of the relay barrel for one of the WFPC1's. Using a set of seven images taken at four field points and two focus positions, we can recover all 10 degrees of freedom of the two-mirror system. We terminated this activity before addressing some key issues, such as detector-noise effects. Nonetheless indications are that it can provide a powerful alternative to conventional interferometric alignment techniques.

The advantages of prescription-retrieval image-based alignment include the following:

- (1) It does not require null lenses, interferometers, or other test optics to align aberrated or aspheric systems.
- (2) As a result it is not susceptible to errors introduced by test optics.
- (3) It is an end-to-end technique that is capable of working in the nominal operational configuration of an instrument including using the science detector.
- (4) It provides alignment over the full operational range of an instrument, i.e., over the full field of view, focus settings, and zoom positions.
- (5) It can be performed remotely, such as during environmental testing of an instrument or during operation of a space instrument.

Conclusion

By using a direct prescription-retrieval image-inversion technique, we have estimated the value of the HST conic constant to be -1.01386 ± 0.0002 . This result agrees with estimates derived from archival data studies. In addition we determined that the relay cameras are slightly aberrated. These aberrations account for discrepancies between the archival

data studies and other studies that used phase-retrieval techniques.

We thank the other members of the Jet Propulsion Laboratory image-inversion team, Mike Shao, Marty Levine, Mark Colavita, Brad Hines, Rich Dekany, and Tony Decou, for their contributions of code and ideas. Others at the Jet Propulsion Laboratory, notably Bob Korechoff and Jim McGuire, were extremely helpful in this work. Si Brewer was extremely generous with his knowledge and insights. This work was performed under contract with NASA.

References

1. L. Furey, T. Dubos, D. Hansen, and J. Samuels-Schwartz, "HST primary mirror characterization," in *Space Optics for Astrophysics and Earth and Planetary Remote Sensing*, Vol. 19 of OSA 1991 Technical Digest Series (Optical Society of America, Washington, D.C., 1991), pp. 14–15.
2. J. Fienup, "HST aberrations and alignment determined by phase retrieval algorithms," in *Space Optics for Astrophysics and Earth and Planetary Remote Sensing*, Vol. 19 of OSA 1991 Technical Digest Series (Optical Society of America, Washington, D.C., 1991), pp. 19–21.
3. M. Shao, "Least-squares image inversion applied to WF/PC II," in *Space Optics for Astrophysics and Earth and Planetary Remote Sensing*, Vol. 19 of OSA 1991 Technical Digest Series (Optical Society of America, Washington, D.C., 1991), pp. 28–29.
4. J. McGuire, Jet Propulsion Laboratory, California Institute of Technology, 4800 Oak Grove Drive, Pasadena, Calif. 91109 (personal communication, 1991).
5. D. Redding, L. Needels, K. Wallace, J. Yu, and M. Levine, *Controlled Optics Modelling Package User Manual, Version 1.0*, JPL Doc. D-9816 (Jet Propulsion Laboratory, California Institute of Technology, 4800 Oak Grove Drive, Pasadena, Calif. 91109, 1992).
6. D. Redding, B. M. Levine, J. W. Yu, J. K. Wallace, "Hybrid ray-trace and diffraction propagation code for analysis of optical systems," in *Design, Modeling and Control of Laser Beam Optics*, Y. Kohanzadeh, G. Lawrence, J. McCoy, and H. Weichel, eds., *Proc. Soc. Photo-Opt. Instrum. Eng.* **1625**, 95–107 (1992).
7. D. Redding and W. Breckenridge, "Optical modeling for dynamics and control analysis," *J. Guidance Control Dyn.* **14**, 1021–1032 (1991).
8. W. Vetterling, S. Teukolsky, W. Press, and B. Flannery, *Numerical Recipes: the Art of Scientific Computing* (Cambridge U. Press, Cambridge, 1985), Chap. 14, p. 521.